Supplementary information

Self-assembled network polymer electrolyte membranes for application in fuel cells at 250°C

SeungJu Lee [1,†], YoungSuk Jo[1,†], Sonjong Hwang[2], Yongha Park[1], YeongCheon Kim[1], Tae Kyung Lee[1], Hyoung-Juhn Kim[1]*, Suk-Woo Nam,[1]* and So Young Lee[1]*

[1] Hydrogen·Fuel Cell Research Center, Korea Institute of Science and Technology, 5, Hwarangro 14-gil, Seongbuk-gu, Seoul 02792, Republic of Korea

[2] Division of Chemistry and Chemical Engineering, California Institute of Technology, Pasadena, California 91125, USA

*Corresponding authors:

S. Y. Lee (Email: sylee5406@kist.re.kr)

S. W. Nam (Email: swn@kist.re.kr)

H. -J. Kim (Email: hjkim25@kist.re.kr)

Content

Supplementary Discussion.

Supplementary Figure.

Supplementary Table.

1. **Cell Performance of comparison of different types of fuel cells as reported in the literature**
2. **Assignment of Raman signals of PA-doped and de-doped SAN-CeHP-PBI**
3. **Properties of representative hydrogen carriers applicable to on-board hydrogen storage system**

Supplementary Discussion.

1. Property for proton conductor: cerium hydrogen phosphate electrolytes

Unlike widely used proton conductors such as tin, titanium, and caesium phosphate, only cerium(IV) phosphate and thorium phosphate are insoluble acid salts of tetravalent metal phosphates forming a fibrous structure[1-3] (**Supplementary Fig. 1a and 1b**). CeHP ($(HCe_2(PO_4)_3(H_2O))$) displays a high proton conductivity (0.018 $S \cdot cm^{-1}$) at 200 °C under dry conditions and is stable up to 300 °C because of the dehydration of the CeHP structure and subsequent condensation reaction of HPO_4^{2-}. Above 300 °C, CeP_2O_7 is formed, affecting the morphology changes (**Supplementary Fig. 1c and 1d**). The solid-state ^{31}P NMR spectroscopic analysis of CeHP and concentrated PA mixtures reveal their solvation behaviour, which is similar to that of an ionomer. With an increase in mixing time, the main peak of CeHP disappeared, whereas the PA and PO_4^{3-} peaks remained. When the mixtures were heated to 250 °C, a condensation reaction occurred, and CeHP reacted with PA to form an amorphous $CeH_xPO_4(OH)_y$ structure. The resultant mixtures containing hydroxyl groups exhibit good affinity to excessive PA and adsorbed water. Their role in the stabilization of proton conduction at a high temperature of 250 °C is shown in **Supplementary Fig. 2**.

2. Acidic proton mobility of the de-doped samples

To exclude the effects of excessive PA doped in the membrane using the sol-gel process, PA was removed by washing the membrane with water (herein called as de-doped membranes) followed by various characterizations. Excessive PA can be removed from the membrane to leave only PA units that are bound via electrostatic bonding to the PBI polymer chains. The total phosphate units/unit mass of the de-doped samples was approximately 3 to 5 times lower than that for the PA-doped samples containing excess PA, as determined from the normalized integration values of the NMR signals. The results indicate that excess PA units are not bonded as the PBI polymer chains are removed **(Supplementary Fig. 7a**). Furthermore, scanning electron microscopy (SEM), energy dispersive X-ray (EDX), and X-ray diffraction (XRD) analyses revealed that in de-doped SAN-CeHP-PBI, the nanofibrous crystalline materials contain CeHP and are connected to each other to form a network. However, in CeHP-PBI, a self-assembled network was not formed, and the CeHP crystals are not closely packed together (**Supplementary Fig. 7b and 7c**). The interference in proton conduction was determined by solid-state ^{31}P NMR spectroscopy. The ^{31}P NMR spectra of the three samples (*p*-PBI, CeHP-PBI, and SAN-CeHP-PBI) demonstrated normalized peaks at 0, -12, and -40 ppm for H_3PO_4, $H_4P_2O_7$ formed by the condensation reaction of two H_3PO_4, and $Ce(PO_4)_2$, respectively (**Supplementary Fig. 7d-f)**. The acidic proton mobility of the de-doped samples was studied in detail via ^{1}H MAS NMR spectroscopy. The ^{1}H MAS NMR spectra were obtained after vacuum dehydration at 130 °C for three different de-doped membranes as shown in **Supplementary Fig. 7g-i**. Note that the presence of H_2O molecules was minimized by vacuum dehydration in order to improve the clarity of ^{1}H resonances. At room temperature, two broad resonances were observed at ~ 12 ppm and ~ 7 ppm with similar signal strengths, which can be assigned to $H_2PO_4^-$ interacting with the imidazole N-H (see proposed structural moiety in **Supplementary Fig. 4b**) and aromatic protons in the polymer backbone[4-6] , respectively. It is likely that the 12 ppm peak corresponds to fast proton exchange between the quarternized imidazole ring N-H (~ 13-14 ppm) and phosphoric acid hydrogen (10.2 ppm for 100% H_3PO_4)[7]. Because of different local structures in the SAN-CeHP-PBI composite membrane in **Supplementary Fig. 7i** (see **Supplementary Fig. 4b**) and **Supplementary Fig. 7g,** an ~10 ppm peak is observed for the N---$HOPO_3^{2-}$ units, but it is not well resolved from the aromatic protons (~ 7 ppm) in PBI, unlike the cases of the other two de-doped membranes (**Supplementary Fig. 7g and 7h**). When three different membranes were investigated with *in-*

situ variable temperature (VT) ^{31}P MAS NMR (see **Supplementary Fig. 7g-i**), noticeable line narrowing was observed for the acidic protons at high temperatures, while the aromatic protons nearly remained unchanged up to 270 °C. The increased tumbling motion of PO_4 units and consequent elimination of anisotropic interactions of ^{1}H spins should be responsible for this motional narrowing as temperature rises. No line narrowing was observed for the aromatic proton resonance, which is consistent with the limited motion of the polymer backbone even at high T. In addition to these two different types of proton resonances, a strikingly narrow resonance appeared at around 0 ppm, and it became increasingly strong with the temperature, suggesting the production of a proton species/moiety with high mobility in a shielded environment. Among the three membrane samples that underwent the same *in-situ* NMR examination, SAN-CeHP-PBI showed the most intense 0 ppm resonance, approximately 3-5 times stronger than that of the other membranes, displayed in **Supplementary Fig. 7g and 7i**. Upon cooling down from the VT exposure, the 0 ppm resonance disappeared, and the room temperature ^{1}H MAS NMR spectra were reproduced. The 0 ppm resonance is yet to be characterized; however, the combination of H_3PO_4 and the imidazole-based polymer membrane may have generated such highly mobile H^+ species at temperatures higher than 200 °C. Furthermore, the dispersed CeHP nanofibrous structure certainly plays a catalytic role in facilitating such generation. Upon examining the CeHP powder based on the same experimental procedure, we observed the same sharp resonance, at ~0.4 ppm; this resonance appeared from approximately 80 °C and intensified rapidly with an increase in temperature (**Supplementary Fig. 7j)**. More importantly, the high proton conductivity of the SAN-CeHP-PBI membrane is well correlated with the concentration of the highly mobile H^+ species.

3. Conceptual design of HT-PEMFC system integrated with hydrogen extraction from liquid hydrogen carrier

Recently, liquid hydrogen carriers (LHCs) have emerged as promising alternatives to conventional compressed hydrogen owing to their high volumetric energy density and compatibility with existing storage and transport infrastructure. The energy density of LHCs, especially methanol, is 5–7 times that of compressed H_2. **Supplementary Fig. 11a** lists several potential LHC candidates for application in on-board H_2 storage systems; the thermodynamic temperature required for 99% conversion and the kinetic temperature range in which the catalytic reactions of these LHC candidates occur are presented in **Supplementary Table 3**. The conceptual design of power generation systems based on PEMFC integrated with a H_2 extraction system using LHCs is shown **Supplementary Fig. 11b**. This demonstrates the applicability of high-efficiency direct LHC fuel cells in energy conversion systems, eliminating the need for additional heat exchangers and a separate fuel processor. Additionally, it allows the integration of the exothermic electrochemical reaction in the fuel cell and the endothermic dehydrogenation reaction, thereby increasing the overall thermal efficiency and shifting the H_2 extraction equilibrium towards a favourable direction by *in-situ* H_2 removal, thus lowering the reaction temperature and increasing the H_2 extraction rate. In the ultimate target configuration for the direct LHC fuel cell, hydrogen-rich LHC is fed to the anode side, where catalysts are packed for internal reforming. This can be realized by packing catalysts in the anode channel, or by coating the catalysts on the anode along with anode catalysts. However, in a single cell, it is difficult to experimentally demonstrate the effects of heat and mass transfer integration, as heat loss is more significant than exchanged heat, and mass transfer enhancement requires designing the flow channels depending on the reaction conditions and catalyst type. Therefore, external reforming was pursued in this experiment by physically attaching the reforming unit to the single-cell while maintaining the same temperature to simulate a heat integrated configuration (**Supplementary Fig. 11c and 11d**).

Supplementary Figure.

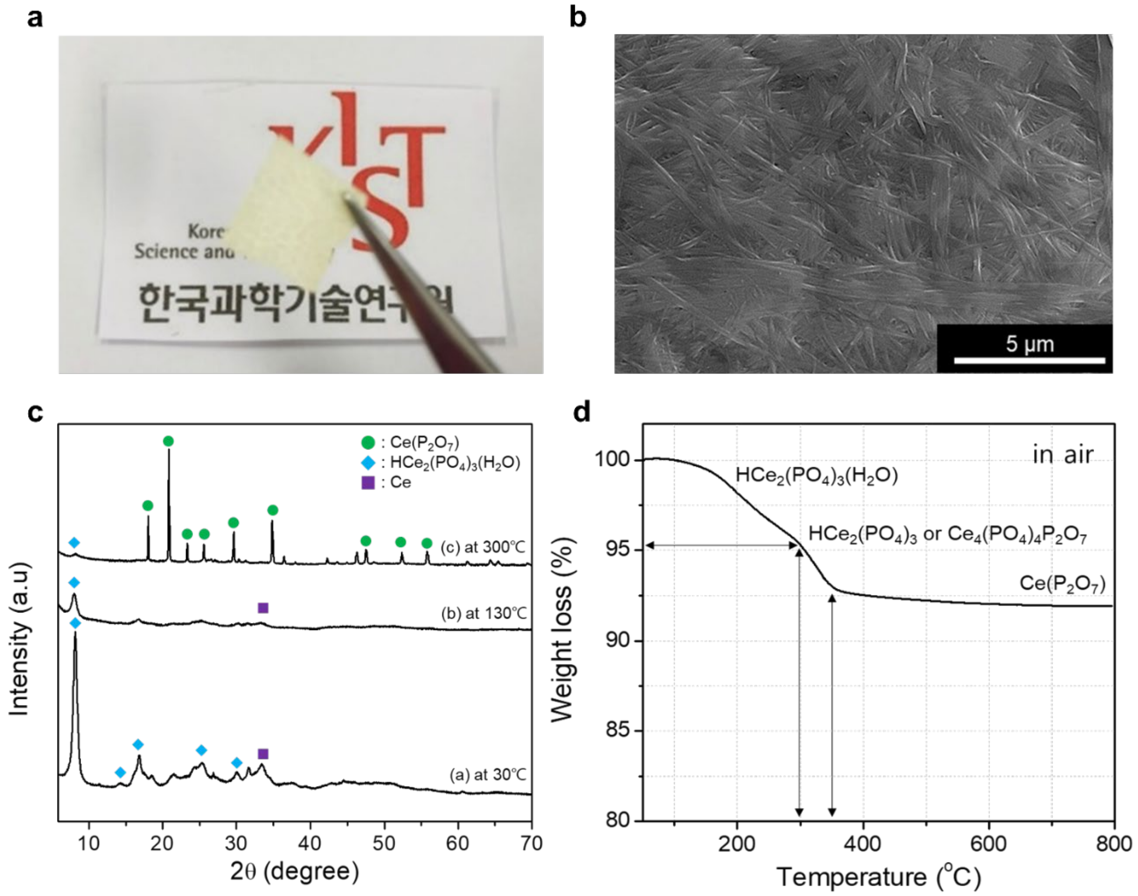

Supplementary Figure 1 | Cerium hydrogen phosphate (CeHP). a, CeHP image. **b,** SEM image of CeHP surface. **c,** XRD profiles of CeHP at different temperatures: (a) initial product, (b) heated at 130 °C, and (c) heated at 300 °C. **d,** Thermogravimetric analysis (TGA) profile of CeHP.

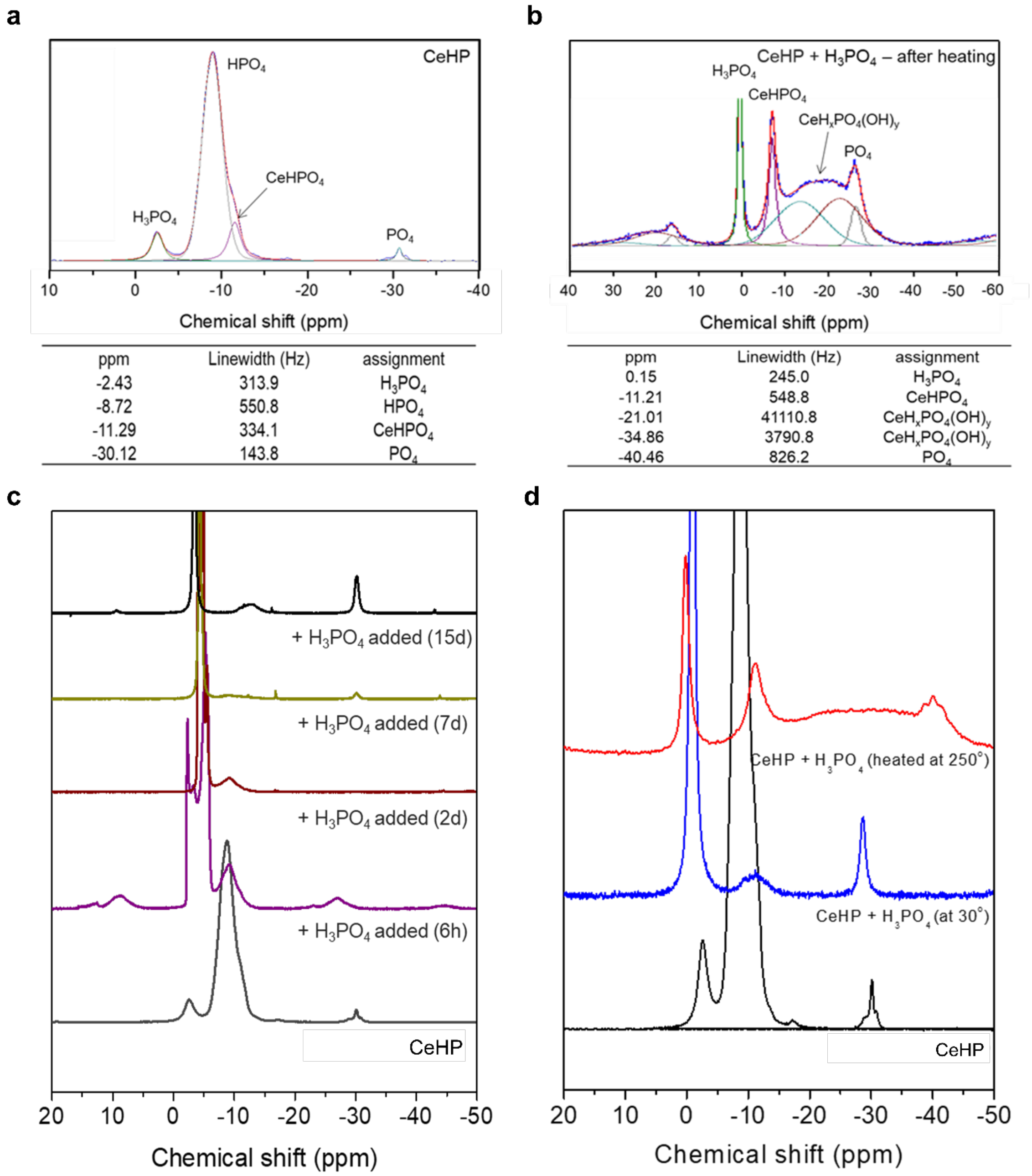

ppm	Linewidth (Hz)	assignment
-2.43	313.9	H_3PO_4
-8.72	550.8	HPO_4
-11.29	334.1	$CeHPO_4$
-30.12	143.8	PO_4

ppm	Linewidth (Hz)	assignment
0.15	245.0	H_3PO_4
-11.21	548.8	$CeHPO_4$
-21.01	41110.8	$CeH_xPO_4(OH)_y$
-34.86	3790.8	$CeH_xPO_4(OH)_y$
-40.46	826.2	PO_4

Supplementary Figure 2 | Solvation behavior of CeHP ionomer mixed with concentrated H_3PO_4. a–d, Solid-state ^{31}P MAS NMR spectra of CeHP ionomer: (a) CeHP ionomer mixed with concentrated H_3PO_4, (b) after heating at 250 °C, (c) mixed for different times, and (d) mixed at different temperatures.

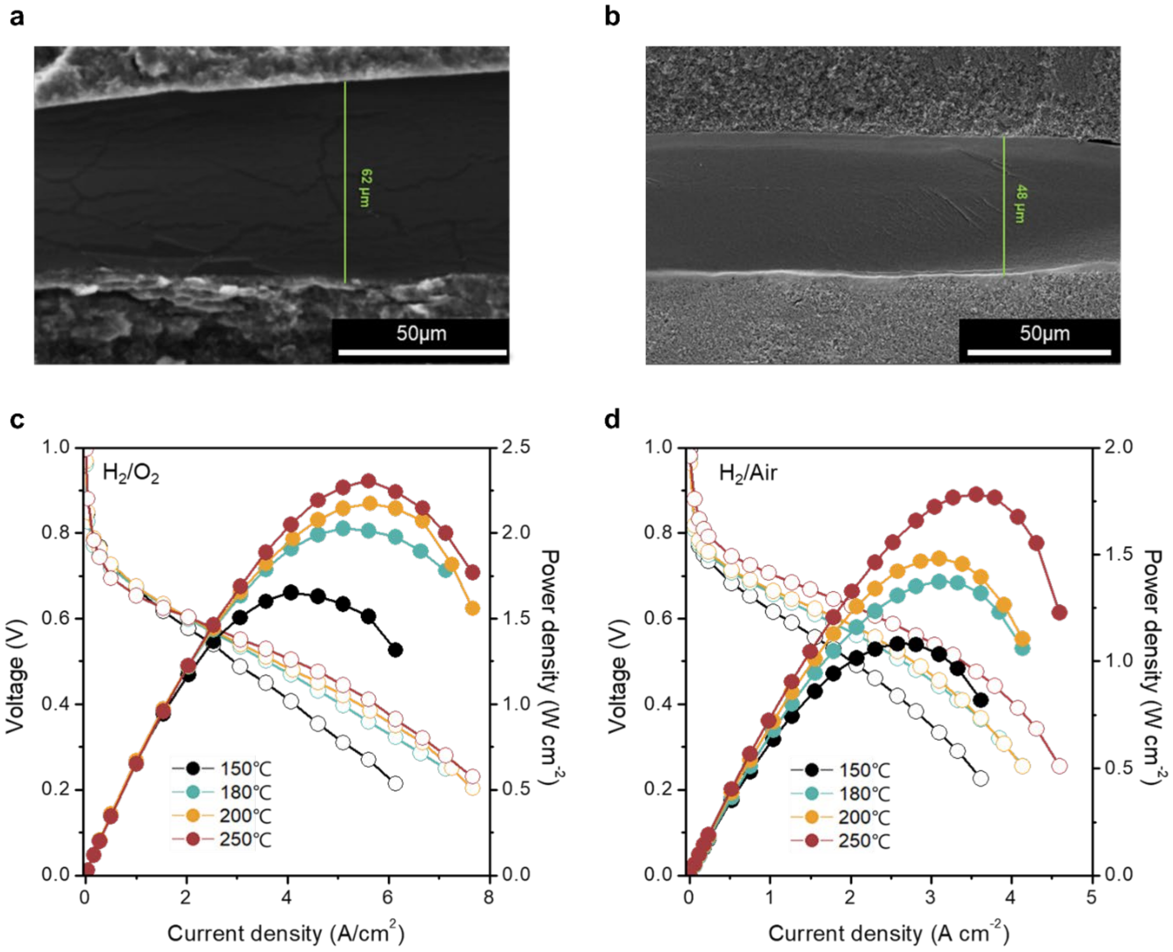

Supplementary Figure 3 | Fuel cell test of SAN-CeHP-PBI. a-b, Scanning electron microscope images of PA-doped SAN-CeHP-PBI composite membrane after 100h at (a) 150°C and (b) 250 °C of fuel cell testing. **c-d,** Fuel cell performance, *i*-V curve with Pt/C (1.5 $\mathrm{mg_{Pt}{\cdot}cm^{-2}}$) and the PA-doped SAN-CeHP-PBI composite membrane (*t* = 110µm) using (c) H_2/O_2 and (d) H_2/Air at 150-250°C under 3 bar without humidification.

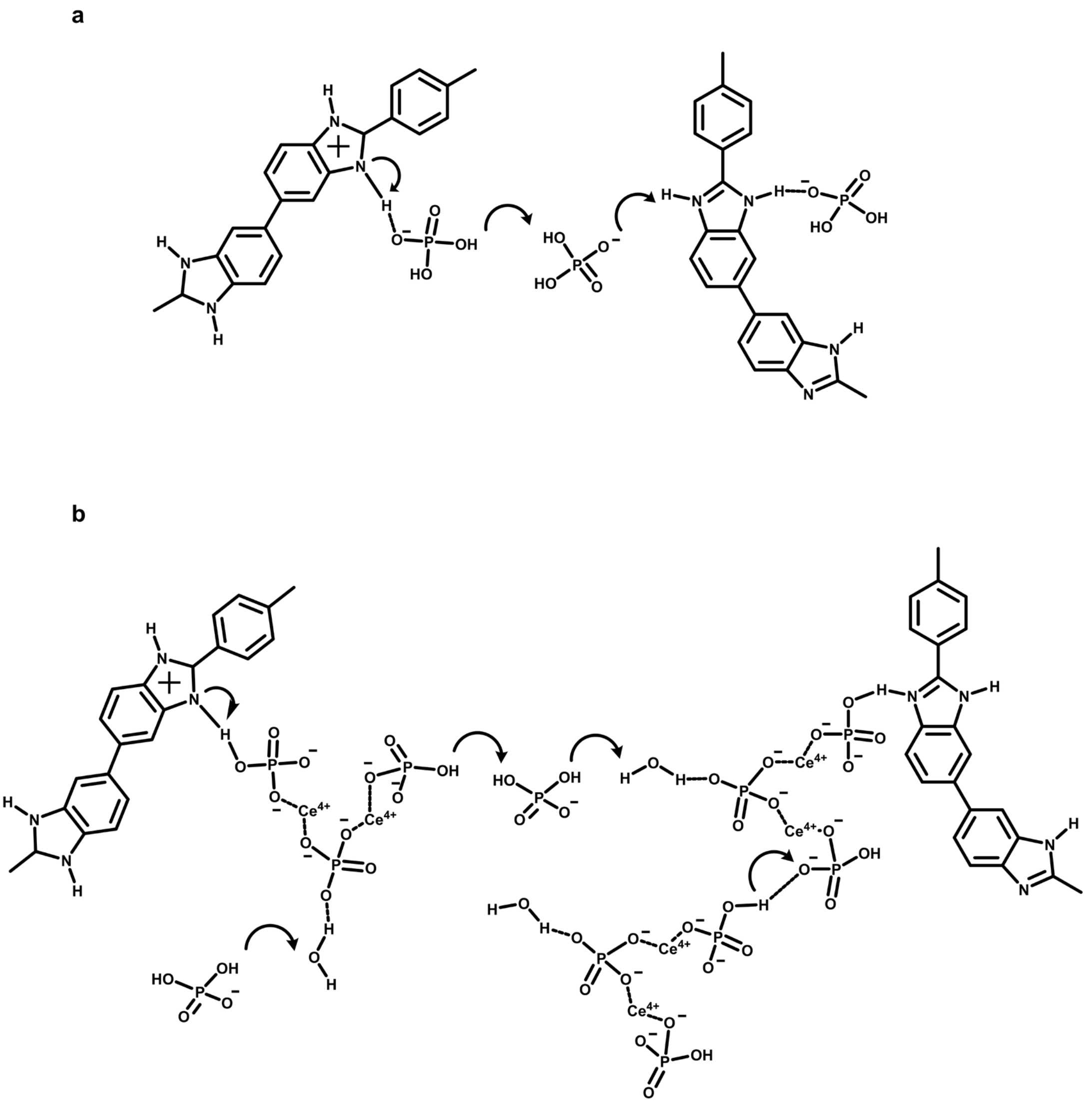

Supplementary Figure 4 | Proton conductivity mechanisms. a–b, (a) *p*-PBI; Grotthus-type hopping mechanism via benzimidazole ring between H_3PO_4 molecules at below 180 °C. (b) SAN-CeHP-PBI composite membrane; a surface/interfacial conduction via proton transfer between benzimidazole ring–cerium hydrogen phosphate and cerium hydrogen phosphate molecules at elevated high temperature of over 200 °C.

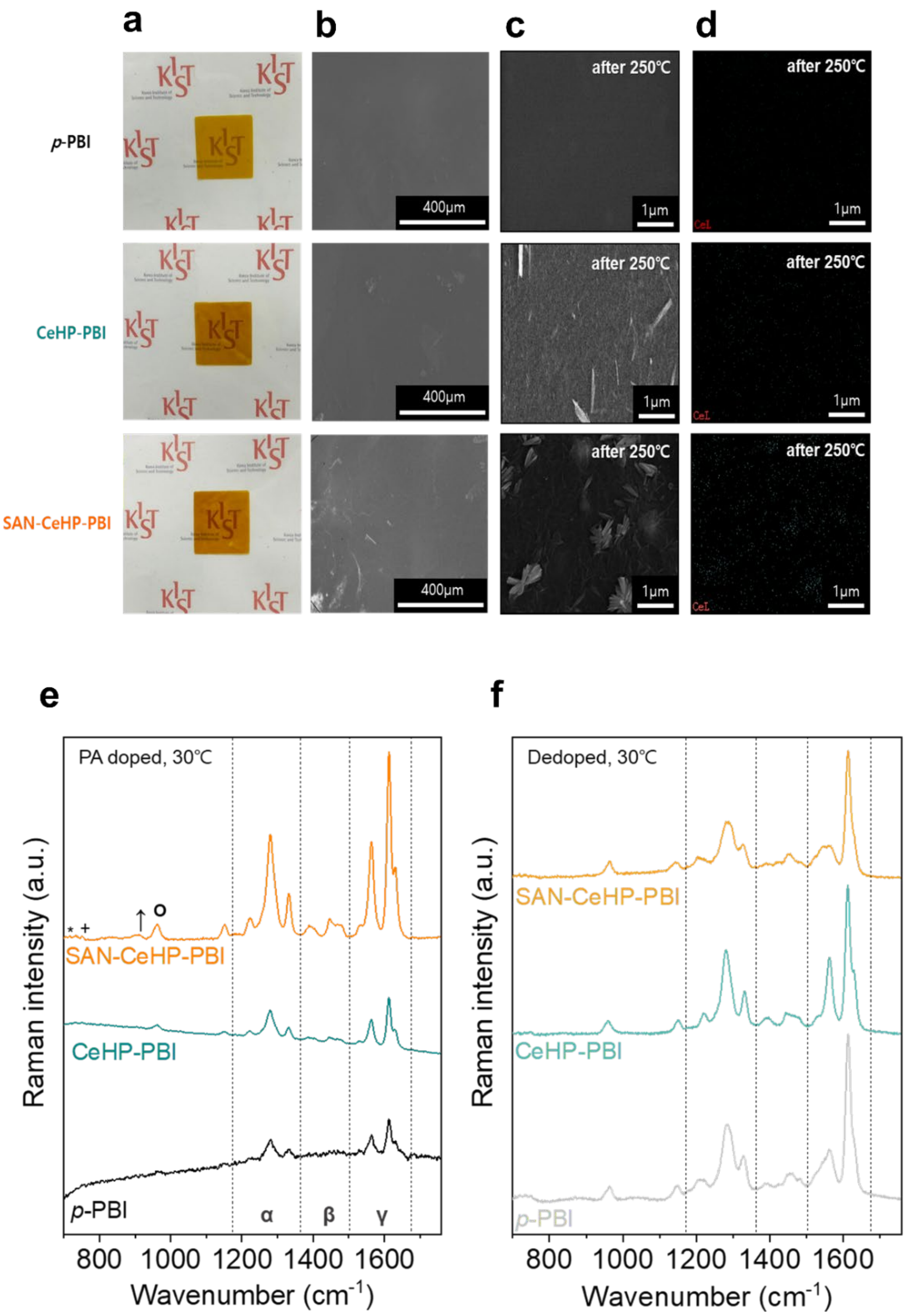

Supplementary Figure 5 | Structural change of PA-doped PBI membranes according to temperature. a, Membrane images of the *p*-PBI membrane, CeHP-PBI composite membrane, and SAN-CeHP-PBI composite membranes. **b-c,** Scanning electron microscope images of (b) before and (c) after 100h of heating at 250 °C for all three samples. **d,** EDX mapping images after 100h of heating at 250 °C of Ce element for all three samples. **e–g,** Raman spectra of *p*-PBI membrane, CeHP-PBI composite membrane, and SAN-CeHP-PBI composite membrane at (e) 30 °C and (f) after de-doped at 30 °C.

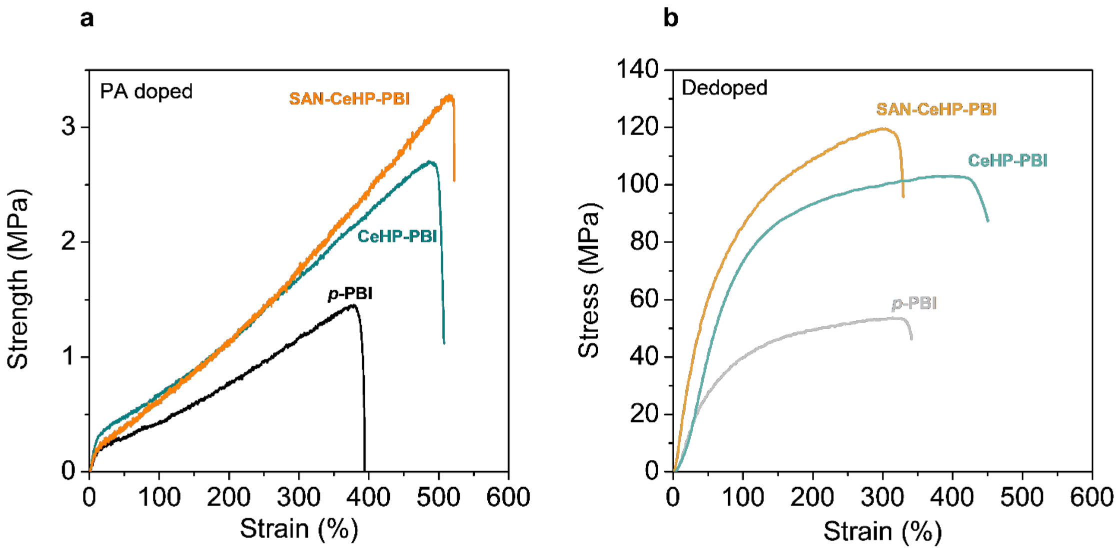

Supplementary Figure 6 | Mechanical stability property of PBI membranes. a-b, Tensile property comparison (a) PA-doped and (b) De-doped among *p*-PBI membrane, CeHP-PBI composite membrane, and SAN-CeHP-PBI composite membrane

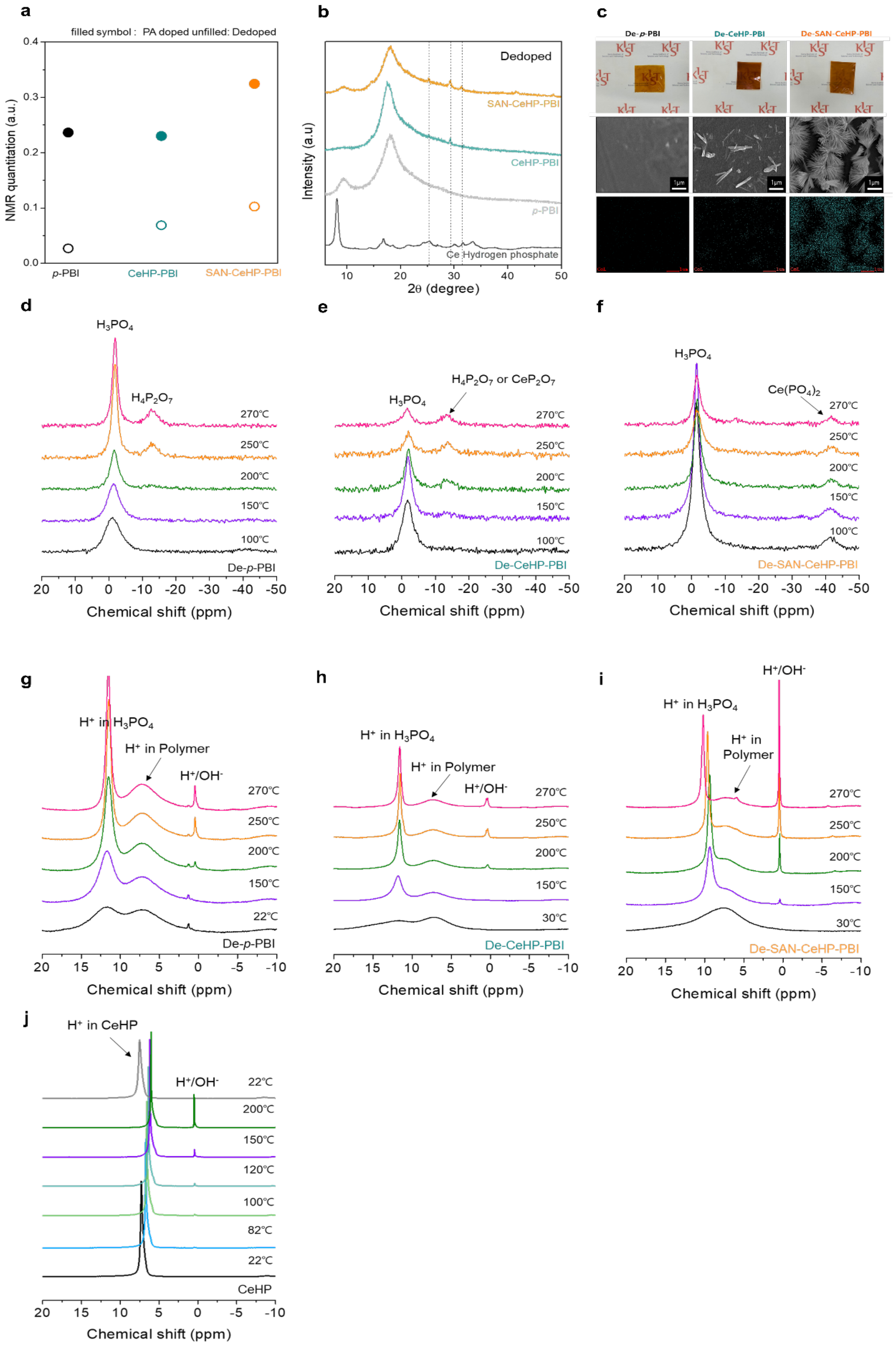
a
filled symbol : PA doped unfilled: Dedoped
NMR quantitation (a.u.)
0.0
0.1
0.2
0.3
0.4
p-PBI
CeHP-PBI
SAN-CeHP-PBI
b
Dedoped
SAN-CeHP-PBI
CeHP-PBI
p-PBI
Ce Hydrogen phosphate
Intensity (a.u)
10
20
30
40
50
2θ (degree)
c
De-p-PBI
De-CeHP-PBI
De-SAN-CeHP-PBI
1μm
d
H3PO4
H4P2O7
270℃
250℃
200℃
150℃
100℃
De-p-PBI
Chemical shift (ppm)
e
H4P2O7 or CeP2O7
H3PO4
270℃
250℃
200℃
150℃
100℃
De-CeHP-PBI
Chemical shift (ppm)
f
H3PO4
Ce(PO4)2
270℃
250℃
200℃
150℃
100℃
De-SAN-CeHP-PBI
Chemical shift (ppm)
g
H+ in H3PO4
H+ in Polymer
H+/OH-
270℃
250℃
200℃
150℃
22℃
De-p-PBI
Chemical shift (ppm)
h
H+ in H3PO4
H+ in Polymer
H+/OH-
270℃
250℃
200℃
150℃
30℃
De-CeHP-PBI
Chemical shift (ppm)
i
H+/OH-
H+ in H3PO4
H+ in Polymer
270℃
250℃
200℃
150℃
30℃
De-SAN-CeHP-PBI
Chemical shift (ppm)
j
H+ in CeHP
H+/OH-
22℃
200℃
150℃
120℃
100℃
82℃
22℃
CeHP
Chemical shift (ppm)

Supplementary Figure 7 | Acidic proton mobility of the de-doped PBI membranes. a, NMR quantitation of total ^{31}P signal among H_3PO_4, HPO_4, PO_4 phases normalized by weight of all three samples; filled symbol; PA-doped; unfilled: De-doped. **b,** XRD profiles of De-doped *p*-PBI membrane, CeHP-PBI composite membrane, and SAN-CeHP-PBI composite membrane. **c,** Membrane images, scanning electron microscope images, and EDX mapping images of Ce element, the De-doped of *p*-PBI membrane, CeHP-PBI composite membrane, and SAN-CeHP-PBI composite membrane. **d-f,** ^{31}P solid-state MAS NMR spectra of De-doped (d) *p*-PBI membrane, (e) CeHP-PBI composite membrane, and (f) SAN-CeHP-PBI composite membrane shown for all four samples as T rises. **h-j,** ^{1}H solid-state MAS NMR spectra of De-doped (h) *p*-PBI membrane, (g) CeHP-PBI composite membrane, and (i) SAN-CeHP-PBI composite membrane and CeHP powder shown for all four samples as temperature rises.

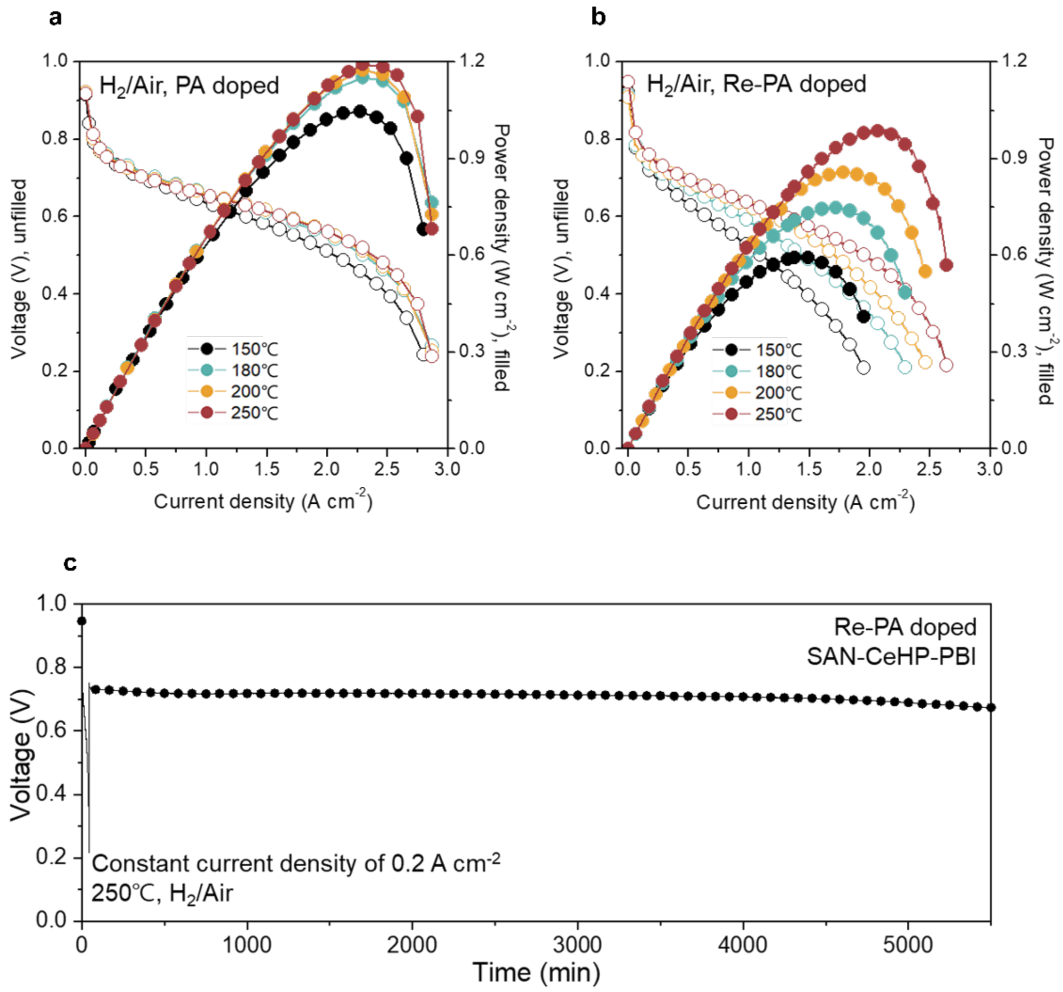

Supplementary Figure 8 | Reversible SAN-CeHP-PBI. a-b, *i*-*V* curve with Pt/C (1.5 $mg_{Pt}\cdot cm^{-2}$) and (a) PA-doped SAN-CeHP-PBI composite membrane (t = 110 μm) and (b) Re-PA-doped SAN-CeHP-PBI composite membrane (t = 120 μm), soaked in water for 3 days and then immersed in 85% PA for 1 day at 30 °C, using H_2/air with no backpressure at 150–250 °C. **c,** Long-term stability of Re-PA-doped SAN-CeHP-PBI composite membrane (t = 120 μm) with Pt/C (1.5 $mg_{Pt}\cdot cm^{-2}$). The fuel cells were tested at a constant current density of 0.2 $A\cdot cm^{-2}$ at 250 °C in H_2/air under anhydrous conditions.

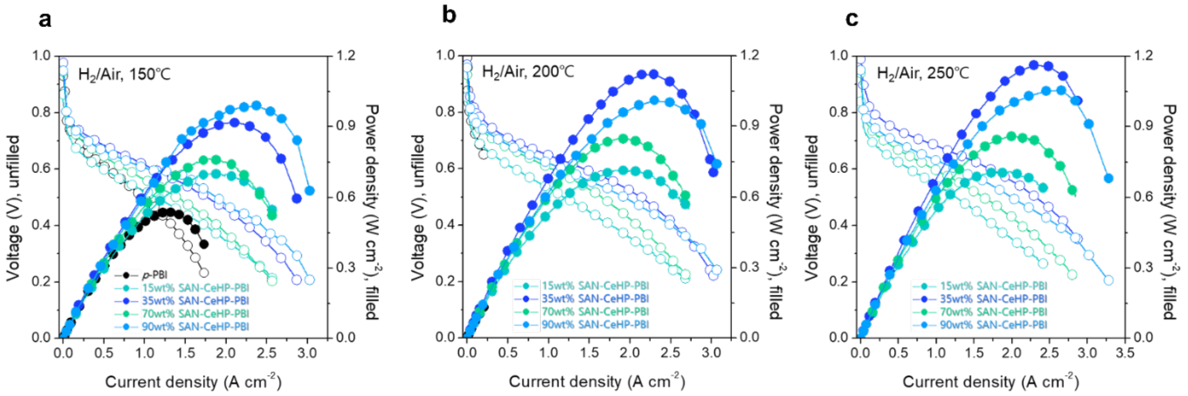

Supplementary Figure 9 | Effect of cerium content on the fuel cell performance of composite membranes. a-c, H_2/Air fuel cell performance, *i*-V curve with the various PA-doped SAN-CeHP-PBI composite membranes with 15, 35, 70 and 90 wt% Cerium precursor ($t = 110\mu m$), with Pt/C (2.0 $mg_{Pt} \cdot cm^{-2}$, BASF commercial electrode) no backpressure at (a) 150, (b) 200 and (c) 250 °C.

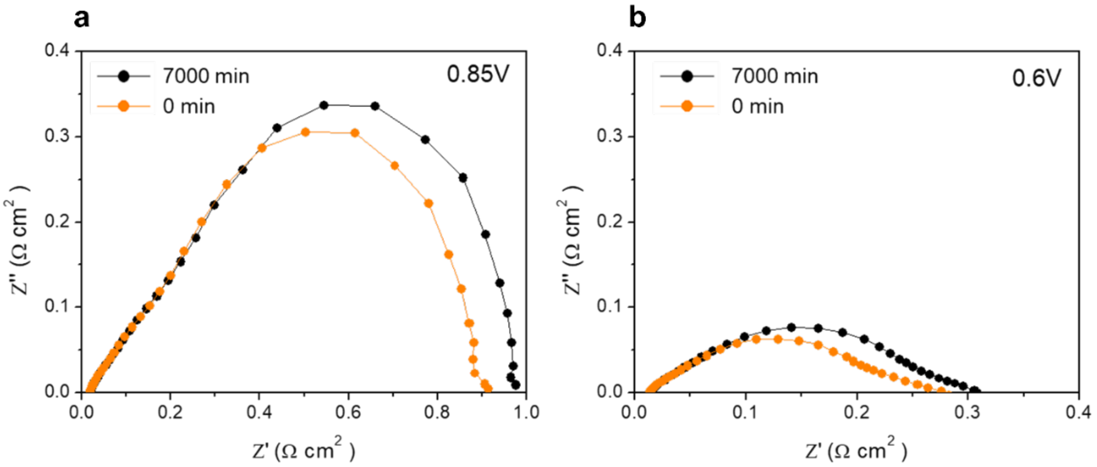

Supplementary Figure 10 | Electrochemical analysis of 35wt% SAN-CeHP-PBI composite membranes. a-b, Electrochemical impedance spectroscopy of PA-doped 35wt% SAN-CeHP-PBI composite membranes before and after 7000min operation at a current density of 0.2 A·cm^{-2} and measured (a) 0.85V and (b) 0.6V

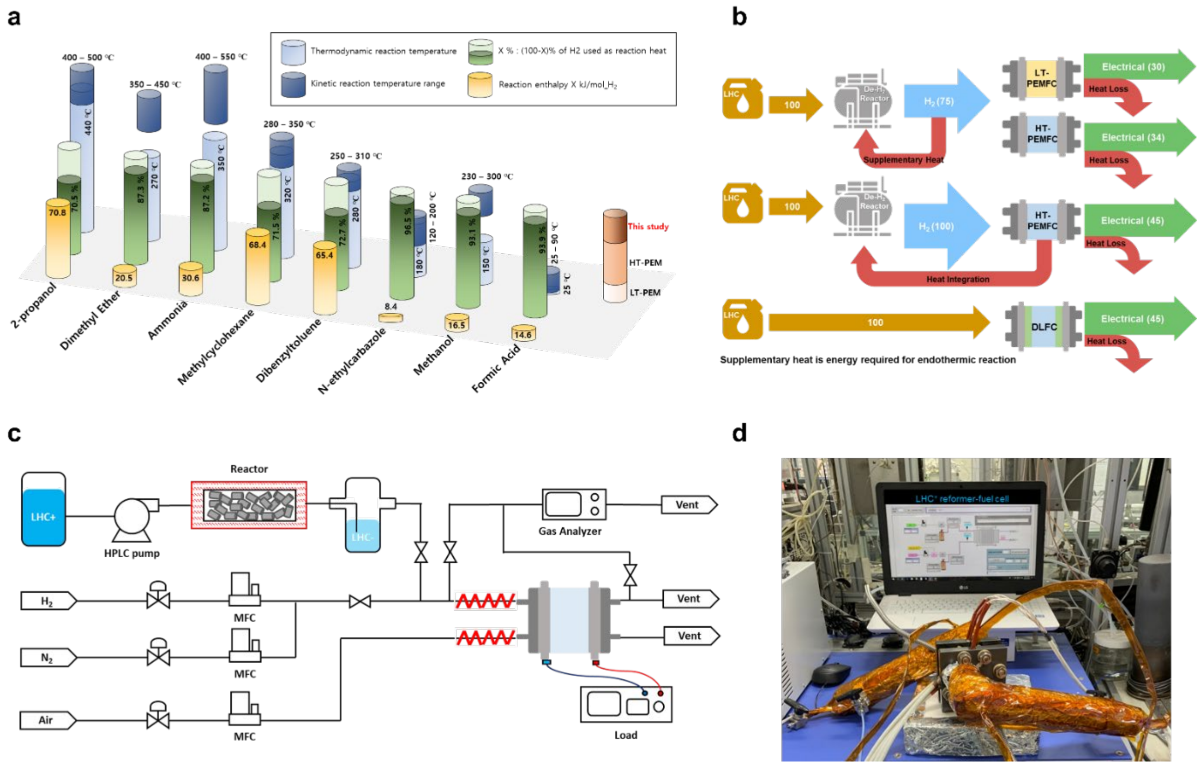

Supplementary Figure 11 | Conceptual design of an integrated HT-PEMFC for power generation systems. a, Properties of representative hydrogen carriers applicable to the on-board hydrogen storage system. Thermodynamic reaction temperature required for > 99% conversion with a reported range of kinetic reaction temperature range for > 60% conversion with varying catalysts in the literature and theoretical reaction enthalpy of hydrogen extraction reaction of the candidates with a proportion of extracted hydrogen required to provide the theoretical reaction heat. **b,** Theoretical energy efficiency comparison with low, high-temperature polymer electrolyte membrane fuel cells and direct liquid hydrogen carrier fuel cells as a source of liquid hydrogen carrier for electricity generation from fuel cells. **c-d,** (c) Schematic diagram, and (d) image of the experimental system LHC (methanol and N-ethylcarbazole) reforming or dehydrogenation in conjunction with a unit cell using PA-doped 35wt% SAN-CeHP-PBI composite membrane (t = 110 μm).

Supplementary Table.

Supplementary Table 1 | Cell Performance of comparison of different types of fuel cells as reported in the literature.

Membranes	Fuel cell	Temperature	Peak power density [W cm^{-2}]	Pt loading [mg cm^{-2}]	Fuel	Conductivity [S cm^{-1}]	Ref
Plasma-coated BPSH membrane	LT-PEMFC	80-120	0.45 (120°C)	1.0	H_2/air	0.51 (80°C RH 100%)	2
PBI/H_3PO_4	HT-PEMFC	140-180	0.60 (180°C)	0.5	H_2/air	0.083 (150°C)	30
TiO_2 composite PBI/H_3PO_4	HT-PEMFC	125-175	1 (175°C)	1	H_2/O_2	0.075 (175°C)	15
$TiSO_4$ composite PBI/ H_3PO_4	HT-PEMFC	150	0.60 (150°C)	1	H_2/O_2	0.048 (150°C)	31
SiO_2 nanoparticles composite PBI/H_3PO_4	HT-PEMFC	160	0.5 (160°C)	1.2	H_2/O_2	0.02 (160°C)	14
Cross-linked PBI/ H_3PO_4	HT-PEMFC	160	0.53 (160°C)	0.6	H_2/O_2	0.253 (200°C)	32
PWA meso-silica composite PBI/ H_3PO_4	HT-PEMFC	200	0.38(200°C)	1.7	H_2/air	0.023 (200°C)	16
QAPOH/ H_3PO_4	HT-PEMFC	120-240	1.74 (240°C)	1.1	H_2/O_2	0.023 (220°C)	18
SnP_2O_7–Nafion composite membrane	IT-PEMFC	200-240	0.87 (240°C)	1.2	H_2/O_2	0.102 (290°C)	17
Ce0.9Gd0.1P_2O_7 composite PBI/ H_3PO_4	IT-PEMFC	160-250	0.31 (160°C)	1	H_2/air	0.182 (180°C)	33
CeP_2O_7 electrolyte membranes	IT-FC(SCFC)	150-250	0.025 (200°C)	1.2mm	H_2/O_2	0.018 (200°C)	34
Molten $CsH_5(PO_4)_2$ electrolyte composite/ PBI	IT-FC(MCFC)	150-250	0.12 (200°C)	0.5	H_2/O_2	0.064 (250°C)	35
CsH_2PO_4-ZrO_2 composite electrolytes	IT-FC	250-275	0.040 (275°C)	0.7	H_2/air	0.02 (250°C)	36
In^{3+}-Doped SnP_2O_7 electrolyte membranes	IT-FC(SCFC)	250	0.265 (250°C)	0.6	H_2/O_2	0.195 (250°C)	37
Thin CsH_2PO_4 electrolyte membranes	IT-FC(SCFC)	240	0.415 (240°C)	0.77	H_2/O_2	0.01 (230°C)	38
	PCFC	≥350 (350-600)	0.10 (350°C)		H_2/air		39
Ceria-based solid electrolyte	SOFC	>800(400-800)	0.10 (350°C)		H_2/air		40
SAN-CeHP-PBI/ H_3PO_4	This work	150-250	2.4 (250°C)	1.5	H_2/O_2	0.257 (280°C)	
SAN-CeHP-PBI/ H_3PO_4	This work	150-250	1.8 (250°C)	1.5	H2/air	0.257 (280°C)	

Supplementary Table 2 | Assignment of Raman signals of PA-doped and de-doped SAN-CeHP-PBI.

Symbol	**PA-doped SAN-CeHP-PBI**	**De-doped SAN-CeHP -PBI**	**Assignment**
+	728	-	C–H out-of-plane ring deformation
	-	905	Stretching mode of PO_4 (ν1)
↑	911	-	Free phosphoric acid
O	964	964	Ring breathing vibration of benzene ring
	1144, 1120	1144	C-C skeletal stretching
	-	1218	Amide (N-H)
α	1281,1327	1281,1331	C–H in-plane bending vibrations
β	1390,1420,1454	1395,1443,1474	C=C/C=N benzimidazole ring stretching vibrations (or C-H in plane vibrations)
γ	1544,1560,1615	1535,1562,1612,1632	C=C/C=N benzimidazole ring stretching vibrations

Supplementary Table 3 | Properties of representative hydrogen carriers applicable to on-board hydrogen storage system.

Thermodynamic reaction temperatures required for > 99% and > 95% of the degree of dehydrogenation (DoDH) are estimated by either calculation or from the literature. Literature data on kinetic reaction temperatures for over 60% conversion of the reactant to hydrogen is listed, and the range denotes different DoDH with different catalysts. Moreover, the heat of reaction and reaction stoichiometry are listed.

Name of H_2 carrier	Abbreviation	T (DoDH 95%) [°C]	T (DoDH 99%) [°C]	T (DoDH) Range [°C]		Heat of Reaction [kJ /mol_H_2]	Reaction stoichiometry
Ammonia	NH_3	250*	350*	400 [1][2]	550 [1][2]	30.60*	$2NH_3 \rightarrow 3H_2 + N_2$
Methane	CH_4	800*	1050*	800 (1 bar) [3] 800 (5~20bar) [3]	900 (1bar) [3] 1000 (5~20bar) [3]	68.60*	$CH_4 + H_2O \rightarrow CO + 3H_2$
2-propanol	C_3H_8O	400*	440*	400 [4][5]	500 [4][5]	70.80*	$CH_3CH(OH)CH_3 + 2H_2O \rightarrow 6H_2 + 3CO$
		380*	600*			33.50*	$CH_3CH(OH)CH_3 + 5H_2O \rightarrow 9H_2 + 3CO_2$
Formic acid	HCOOH	X	X	25 [6][7]	90 [6][7]	14.60*	$HCOOH \rightarrow H_2 + CO_2$
Formate (Na)	$Na^+ HCOO^-$	X	X	30 [8]	80 [8]	20.50	$NaHCOO + H_2O \rightarrow NaHCO_3 + H_2$
Methylcyclohexane	MCH	300*	320*	280 [9]	350 [9]	68.30*	$C_7H_{14} \rightarrow C_7H_8 + 3H_2$
Dibenzyltoluene	DBT	270	280	250 [10]	310 [10]	65.40	$C_{18}H_{36} \rightarrow C_{18}H_{18} + 9H_2$
N-ethylcarbazole	NEC	174	180	120 [11]	200 [11]	8.40	$C_{14}H_{25}N \rightarrow C_{14}H_{13}N + 6H_2$
Dimethyl Ether	DME	170*	270*	350 [12]	450 [12]	20.5*	$CH_3OCH_3 + 3H_2O \rightarrow 2CO_2 + 6H_2$
Methanol	MeOH	60*	150*	230 [13]	300 [13]	16.5*	$CH_3OH + H_2O \rightarrow CO_2 + 3H_2$

* calculated using Peng-Robinson equation of state in Aspen plus v 11.

References for Supplementary information

1 Albert, G. & Costantino, U. Crystalline insoluble acid salts of tetravalent metals: X. Fibrous thorium phophate, a new inorganic ion-exchange material suitable for making (support-free) inorganic sheets. *Journal of Chromatography A* **50**, 482-486 (1970).

2 Alberti, G., Constantino, U., Di Gregorio, F., Galli, P. & Torracca, E. Crystalline insoluble salts of polybasic metals-III: Preparation and ion exchange properties of cerium (IV) phosphate of various crystallinities. *Journal of Inorganic and Nuclear Chemistry* **30**, 295-304 (1968).

3 Shakshooki, S., El-Akari, F., El-Fituri, S. & El-Fituri, S. in *Advanced Materials Research.* 3-8 (Trans Tech Publ).

4 Bhavsar, R. S., Kumbharkar, S. C., Rewar, A. S. & Kharul, U. K. Polybenzimidazole based film forming polymeric ionic liquids: synthesis and effects of cation–anion variation on their physical properties. *Polymer Chemistry* **5**, 4083-4096 (2014).

5 Zhao, L. *et al.* Imidazole-doped cellulose as membrane for fuel cells: structural and dynamic insights from solid-state NMR. *The Journal of Physical Chemistry C* **120**, 19574-19585 (2016).

6 Goward, G. R., Schuster, M. F., Sebastiani, D., Schnell, I. & Spiess, H. W. High-resolution solid-state NMR studies of imidazole-based proton conductors: Structure motifs and chemical exchange from 1H NMR. *The Journal of Physical Chemistry B* **106**, 9322-9334 (2002).

7 Wasmus, S., Valeriu, A., Mateescu, G., Tryk, D. & Savinell, R. Characterization of H3PO4-equilibrated Nafion® 117 membranes using 1H and 31P NMR spectroscopy. *Solid State Ionics* **80**, 87-92 (1995).

8 Wang, S. *et al.* Investigation on modification of Ru/CNTs catalyst for the generation of COx-free hydrogen from ammonia. *Applied Catalysis B: Environmental* **52**, 287-299 (2004).

9 Cha, J. *et al.* Ammonia as an efficient COX-free hydrogen carrier: Fundamentals and feasibility analyses for fuel cell applications. *Applied energy* **224**, 194-204 (2018).

10 Meloni, E., Martino, M. & Palma, V. A short review on Ni based catalysts and related engineering issues for methane steam reforming. *Catalysts* **10**, 352 (2020).

11 Mizuno, T. & Nakajima, T. TPR studies on steam reforming of 2-propanol on Rh/Al 2 O 3, Ru/Al 2 O 3 and Pd/Al 2 O 3. *Reaction Kinetics and Catalysis Letters* **78**, 315-324 (2003).

12 Mizuno, T., Matsumura, Y., Nakajima, T. & Mishima, S. Effect of support on catalytic properties of Rh catalysts for steam reforming of 2-propanol. *International journal of hydrogen energy* **28**, 1393-1399

(2003).

13 Luo, Y. *et al.* Anchoring IrPdAu nanoparticles on NH2-SBA-15 for fast hydrogen production from formic acid at room temperature. *ACS applied materials & interfaces* **12**, 8082-8090 (2020).

14 Stathi, P., Deligiannakis, Y., Avgouropoulos, G. & Louloudi, M. Efficient H2 production from formic acid by a supported iron catalyst on silica. *Applied Catalysis A: General* **498**, 176-184 (2015).

15 Hwang, Y. J. *et al.* Development of an Autothermal Formate-Based Hydrogen Generator: From Optimization of Formate Dehydrogenation Conditions to Thermal Integration with Fuel Cells. *ACS Sustainable Chemistry & Engineering* **8**, 9846-9856 (2020).

16 Hamayun, M. H., Maafa, I. M., Hussain, M. & Aslam, R. Simulation Study to Investigate the Effects of Operational Conditions on Methylcyclohexane Dehydrogenation for Hydrogen Production. *Energies* **13**, 206 (2020).

17 Jorschick, H. *et al.* Hydrogen storage using a hot pressure swing reactor. *Energy & environmental science* **10**, 1652-1659 (2017).

18 Gong, X., Jiang, Z. & Fang, T. Enhancing selectivity and reducing cost for dehydrogenation of dodecahydro-N-ethylcarbazole by supporting platinum on titanium dioxide. *International Journal of Hydrogen Energy* **45**, 6838-6847 (2020).

19 Faungnawakij, K. *et al.* Hydrogen production from dimethyl ether steam reforming over composite catalysts of copper ferrite spinel and alumina. *Applied Catalysis B: Environmental* **74**, 144-151 (2007).

20 Sá, S., Silva, H., Brandão, L., Sousa, J. M. & Mendes, A. Catalysts for methanol steam reforming—A review. *Applied Catalysis B: Environmental* **99**, 43-57 (2010).